THE ASTROPHYSICAL JOURNAL, 439:381–398, 1995 January 20

YOUNG OXYGEN-RICH SUPERNOVA REMNANTS. II. AN OXYGEN-RICH EMISSION MECHANISM

RALPH S. SUTHERLAND[1] AND MICHAEL A. DOPITA[2]
Received 1993 October 29; accepted 1994 June 10

ABSTRACT

An emission mechanism is presented for the observed oxygen-rich plasma emission in young, oxygen-rich supernova remnants (OSNRs). The mechanism involves the interaction of a fast moving "blob" of oxygen-rich material with the SNR medium, forming a bow-shock/cloud-shock structure. The shock emission is then determined to drive a weak R-type ionization front through the oxygen-rich material. The combined shock and ionization front emission reproduces the major features of the observed optical and UV spectrum.

Dynamical constraints based on the observed motions, lifetimes, and estimated densities of the oxygen-rich knots are used to determine model parameters. The plasma composition, predominantly [Ne/O] ≈ -0.34, used is consistent with massive stellar evolution and explosive synthesis models. Significantly, the unusually high [O III] temperature-sensitive ratio is reproduced simultaneously with the low ionization, optical, [O I], and [O II] lines. The UV emission is predicted, and a good comparison is made with the UV spectrum of SNR E102.2−7219 from observations of Blair et al. (1989). Specific abundance variations were not used to make detailed fits to the observations, detailed abundance determination will require further observations.

This forms the second paper in a short series; in the first paper observations for three southern OSNRs were presented. Those observations are used here along with other observations from the literature.

Subject headings: radiation mechanisms: nonthermal — shock waves — supernova remnants

1. BACKGROUND

In the vast majority of cases, astrophysical plasma emission is dominated by emission from ions and molecules of hydrogen. The other elements can generally be considered to be "contamination" in the hydrogen plasma, although some elements such as carbon and oxygen can have a significant impact on the plasma properties, even at the low relative abundance levels observed. A small class of young supernova remnants (SNRs) exists in which emission has been detected from plasma with a very different composition, providing the exception to the hydrogen domination seen elsewhere. The archetypical example is the northern Cas A remnant (cf. Chevalier & Kirshner 1979, and references therein), where emission in some small knots is apparently devoid of hydrogen emission altogether. Some knots show emission from sulfur, argon, and calcium, and others show forbidden line emission, of purely oxygen or oxygen and neon lines. This has been generally interpreted as the excitation of, and emission by, material from the deep layers of a massive star, laid bare by the supernova explosion.

The fragments of oxygen-rich material themselves may have been formed during expected phases of Rayleigh-Taylor (R-T) instability in the interface regions, between layers of different composition, during the early stages (less than 20,000 s) of the supernova explosion. The detailed multidimensional hydrodynamical models by Fryxell, Müller, & Arnett (1991), in particular, suggest that the interface between the oxygen-rich layers and the overlying helium-rich layer will suffer strong R-T instabilities with only small initial perturbations. The resulting "fingers" of core material that penetrate the outer layers also exhibit surface Kelvin-Helmholtz instabilities, which have been assumed will eventually lead to the fragmentation of the fingers into clumps of material. These may then mix with the outer helium and hydrogen layers of the star. With the large oxygen-neon layers expected in the massive star models, it seems reasonable to assume that some of the resulting clumps would be oxygen-neon material, although the details of subsequent mixing and dissipation of the material is still very uncertain. There is also more direct observational evidence of the formation of a "clumpy" distribution of oxygen material in SN 1987A by Stathakis et al. (1991) and Li & McCray (1992). These studies together suggest that the formation of oxygen-rich clouds are a natural consequence of the physics of a massive star supernova explosion.

In Wolf-Rayet (W-R) progenitors, sometimes proposed for the oxygen-rich supernova remnants (OSNRs), the massive outer hydrogen layers of a red giant will not be present. This might help to make the eventual exposure of the oxygen-rich knots more likely to occur before they are dissipated.

At present there are seven OSNRs known: Cas A, SNR G292.0+1.8, Pup A, SNR 0540−69.3, N132D, SNR E102.2−7219, and an anonymous SNR in NGC 4449 (cf. Chevalier 1975; Chevalier & Kirshner 1978; Goss et al. 1979; Murdin & Clark 1979; Winkler & Kirshner 1985; Mathewson et al. 1980; Danzinger & Dennefeld 1976a, b; Lasker 1978; Dopita, Tuohy, & Mathewson 1981; Balick & Heckman 1978; Blair, Kirshner, & Winkler 1983). A summary of observed properties of the OSNR is given in § 2, Tables 1–2.

Despite the small sample, with a range of sizes and ages, a number of consistent features are apparent in the observed emission. With the exception of SNR 0540−69.3, which shows no neon, all display some material with both oxygen and neon line emission. This oxygen-rich material is always present in small, fast-moving knots of material. The limited plasma diagnostics available from the optical line ratios show remarkably similar values for the apparent electron temperature, and to a lesser extent, similar densities. Without a detailed model,

[1] Joint Institute for Laboratory Astrophysics, University of Colorado and National Institute of Standards and Technology, Campus Box 440, Boulder, CO 80309.
[2] Mount Stromlo and Siding Spring Observatories, Australian National University, Private Bag, Western Creek Post Office, ACT 2611, Australia.

however, the interpretations of the measured properties are not particularly well constrained. Unfortunately, when constraints are sought in UV observations, in the hope of detecting more emission lines to constrain the plasma diagnostics, the heavy reddening of the galactic remnants makes them undetectable. Only the relatively unreddened Magellanic remnant SNR E102.2−7219 has had UV spectroscopy published to date (Blair et al 1989). In that case it was clear that a simple photoionization or shock model is inappropriate, again leaving the interpretation of the spectra uncertain.

Our ability to take advantage of these observations and gain an insight into massive star, and supernova nucleosynthetic and explosion processes, therefore depends on our ability to model the emission process in the oxygen-rich clouds. In the past, attempts at modeling the oxygen-rich emission have concentrated largely on the consideration of the passage of fully radiative shocks through these fragments of stellar material. The shocks are assumed to be formed as the fragments, traveling on ballistic trajectories through the SNR, collide with reflected shock waves that are generated as the main SN blast interacts with the circumstellar medium. The pioneering shock modeling investigations cast light upon a number of intrinsic difficulties caused by the unusually extreme composition of the model plasmas.

1.1. *Radiative Shock Models*

In the literature of OSNRs, a natural assumption has been made that the emission is due to slow, fully radiative shocks traveling through the emission knot material. Interestingly, the composition of the oxygen-rich material gives rise to some unusual structures in the shock models, that differ considerably from those of normal radiative shock models. The main feature is the enormous emissivity of the oxygen-rich material, resulting in extremely rapid cooling.

The highly efficient cooling of oxygen and neon ions can give rise to cooling timescales that are much shorter than the recombination timescales of the plasma. This results in the cooler plasma remaining far more highly ionized that expected (Itoh 1981a, b; Dopita, Binette, & Tuohy 1984). The actual ionization state that is frozen into the cooling phase is determined by the competition of postshock ionization and cooling rates, which are of comparable magnitude. The plasma is usually far from equilibrium, even when compared to shock structures of similar temperatures in normal plasmas.

Shocks in oxygen plasma display very low temperatures in the recombination zone, even when the initial shock temperature is very high. For example, the 100 km s^{-1} shock computed here (see § 4) has a postshock temperature of -1.5×10^6 K, but a temperature in the cooled zone of less than 300 K. This large ratio gives rise to very great compression factors, even when moderate magnetic fields are present. High compression causes collisional quenching in sensitive lines, such as [O II] $\lambda\lambda$3726+29. The very low temperatures in the zones where O II and O I ions are formed means that the cooled zone does not radiate the [O II] $\lambda\lambda$3727 or [O I] λ6300 lines that are normally associated with radiative shock models. Dopita et al. (1984) noted that, in their models, most of the [O I] emission actually came from the head of the shock where the gas was being ionized, rather than in the downstream recombination zone.

In pure oxygen plasmas, when the electron temperature drops below a critical level, further cooling may be prevented due to the lack of efficient fine-structure cooling transitions in the p^3 O II ion. This might help produce optical [O II] emission in the recombination zone by maintaining the electron temperature. Unfortunately, when "impurities" such as silicon, carbon, and neon are introduced, many fine-structure channels for cooling exist, and the plasma cools rapidly to temperatures as low as 100 K, cutting off any optical forbidden emission, although recombination emission may possibly still occur.

The simple shock models published to date (such as Dopita et al. 1984) have suffered from these problems and exhibit a number of critical failures when compared to observations.

1. The [O I] λ6300 emission predicted in the models is too weak by orders of magnitude.
2. The predicted value of the [O III] $I_{4363}/(I_{5007} + I_{4959})$ temperature-sensitive ratio is not consistent with the observations.
3. In order to accommodate both the observed [O II]:[O III] I_{3727}/I_{5007} and the [Ne V]:[Ne III] I_{3426}/I_{3869} ratios, the range of model shock velocities is restricted to 120–130 km s^{-1} in all cases (Dopita et al. 1984). This is implausibly restrictive.

The work by Dopita et al. (1984) served to summarize the failings with the simple radiative shock models.

1.2. *Alternative Models*

Various alternatives to the simple radiative shock model have been proposed, having various degrees of success, namely:

1. The oxygen fragments experience "cosmic-ray" heating from $\sim 10^4$ km s^{-1} ions from the upstream medium. This will occur when the clouds are small compared to the ion Larmor radius or the magnetic field is not transverse, allowing ions to penetrate the oxygen-rich material, depositing energy by Coulomb interactions (Dopita et al. 1984).
2. A bow shock, consisting of high-temperature plasma, builds up at the head of the oxygen cloud, creating a soft X-ray radiation field that produces ionization fronts, and shock waves, moving back into the body of the cloud (Dopita 1987, hereafter D87). This requires the cloud to be large enough to permit the formation of the bow-shock/cloud-shock structure.
3. Knots are heated directly by thermal conduction from the surrounding hot material (Chevalier 1975; Dopita et al. 1984).
4. "Normal" radiative shocks pass through the oxygen-rich fragment, with the modification that the effects of electron thermal conduction have a significant effect on the thermal structure of the shock (Borkowski & Shull 1990).

These proposals share the common aim of trying to increase the electron temperature in the zones where O II and O I emission occurs, either the shock recombination tails or in photoionized ionization front zones. The present work is aimed specifically that taking the initial study by D87 of the R-type ionization front mechanism (see § 5) and determining whether the model holds up under a set of more consistent physical conditions. The other models are not considered in the present work and will not be discussed further except when they have direct implications for the present models.

1.2.1. *Ionization Front Models*

In the model of D87, ionization fronts were formed in the oxygen-rich material when this was illuminated by the ionizing field produced by relatively fast ($\gtrsim$500 km s^{-1}) shocks passing through the oxygen-rich material. In that work, the H- and

He-like line emission of a fast oxygen-rich shock was approximated by an appropriate truncated power-law spectrum. Although the equilibrium photoionization temperatures of the irradiated plasmas were around 200–300 K, the initial deposition of energy by hard photons, through direct and Auger ionizations in the neutral plasma, produced a "super-heating" effect. The peak temperature reached several tens of thousands of kelvin in that study. The resulting spectra of the integrated ionization fronts were a significant improvement on the earlier radiative shock models. The low densities inferred for the resulting [O II]-emitting regions is one of the more encouraging aspects of that model.

The present study tests whether a bow-shock/cloud-shock structure in an oxygen-rich medium can, in practice, achieve the conditions necessary to produce such ionization fronts. The formation of a suitable ionizing radiation field is critical to the model, and this role is filled by the shock waves formed in the dynamical interaction. The emission from any resulting ionization fronts will be calculated, and the final spectra will be a sum of the shock and front spectra. The D87 work only considered the optical emission from the ionization front, since the very fast shocks considered there as the source of soft X-rays were unlikely to become radiative at optical wavelengths.

As was shown in Paper I, the observed optical spectral data do not provide strong constraints on the plasma properties when considered as a homogeneous plasma slab. However, some general assumptions about temperatures and densities can be made to begin the modeling; then other global properties, particularly size and observed lifetimes, can be used to constrain the models.

Therefore in the present work we shall proceed:

1. To use the observation data to determine what physical constraints on spatial scales, temperatures, and densities of the oxygen-rich emission material can be made;
2. To use these to describe a bow-shock/cloud-shock model in semiqualitative terms;
3. To investigate the details of the expected shock structures, with particular reference to their cooling timescales and suitability as an ionizing source capable of driving an ionization front;
4. To provide constraints on the structure and properties of the ionization front models;
5. Based on these properties, to examine the parameter space of the modeling problem, to determine the parameters for the final modeling procedure;
6. Finally, to generate models, applicable to the chosen parameter space, and to compare these with the observations.

2. OBSERVATIONAL SUMMARY

The literature of observations of the OSNRs covers multiple wavelengths. The optical spectra provide means to clearly differentiate the oxygen-rich material from other material and give limited temperature and density information. Imaging, photographic and CCD, provides information on morphology. Proper-motion studies, combined with radial velocities from spectroscopy, give space velocity information. UV spectroscopy, when it has been possible, has detected other species (notably carbon, magnesium, and possibly silicon) that do not radiate in the optical in any strength. X-ray observations have been made of some of the OSNRs, and this gives information about the hot phase that fills the SNRs. Information on the SNR plasma pressure and some composition information has been determined. Finally, IR and radio 21 cm observations have proved useful in determining line-of-sight absorption and inferred distances for the galactic remnants, in particular. More recently, the IR emission from dust within the hot X-ray plasma has been modeled (i.e., Dwek 1987; Arendt, Dwek, & Petre 1991), which appreciably augments the X-ray diagnostics. Some selected observations of the OSNRs, concentrating on the global SNR properties and the hot X-ray SNR medium, are summarized in Table 1.

The optical emission from oxygen-rich material has been summarized in Table 2. This table includes observations from the literature (*top*) and the highest quality observations of Paper I (*bottom*). The literature observations have been taken from the published raw observations, and all the spectra have been dereddened using the same reddening curve method of Kaler (1976), for consistency. The normal logarithmic reddening constant formalism is used, where $I = I_0\, 10^{cf(\lambda)}$. The observed intensity for a given line is given by I, the original intensity is I_0, $f(\lambda)$ is the reddening curve, and c is the reddening constant. The curve of Kaler (1976) is based on the Whitford (1958) curve. When reddening has been expressed in other works in terms of A_v extinction of $E(B-V)$ color excess,

TABLE 1

OXYGEN-RICH SNR DIMENSIONS

SNR	Distance (kpc)	Diameter[a] (pc)	L_X[b] ($\times 10^{36}$ ergs s^{-1})	T_X[c] ($\times 10^6$ K)	n_e[d] (cm^{-3})	Age ($\times 10^{10}$ s)	References
Cas A	2.9	1.3–1.7	5	7.5/33	10–60	1.3	1, 2
Pup A	1.8–2	12–14	~1	1–15	0.3–1	11.0	3, 4, 5
SNR G292.0+1.8	3.6	3(6)	1.3	6/46	1	4.7	6, 7, 8
N132D	50	6/32(80)	45–83	6.6/46	1.6	4.1	9, 10, 11
SNR 0540−69.3	50	2	8.4	...	...	2.4	7, 10, 12
SNR E102.2−7219	60	7(12)	15–20	6/46	3.6	6.8	13, 14

[a] A range is given for noncircular shapes. Parentheses enclose values for outer structures such as diffuse halos. Slashes separate radii for structures in the main SNR.

[b] These are fairly uncertain. These refer to various bands in the 1–20 keV range, mostly 0.2–4.5 keV from *Einstein* observations.

[c] These are fairly uncertain. Slashes separate temperatures for two-component fits.

[d] The older references often make assumptions about collisional ionization equilibrium (CIE) ionization and may overestimate the densities, as a result.

REFERENCES—(1) Fabian et al. 1980; (2) Jansen et al. 1988; (3) Winkler et al. 1981; (4) Winkler et al. 1983; (5) Arendt et al. 1991; (6) Clark, Tuohy, & Becker 1980; (7) Clark et al. 1982; (8) Tuohy, Clark, & Burton 1982; (9) Lasker 1978; (10) Long, Helfand, & Grabelsky 1981; (11) Hughes 1987; (12) Seward & Harnden 1984; (13) Seward & Mitchell 1981; (14) Dopita & Tuohy 1984.

TABLE 2

OXYGEN-RICH REMNANT OBSERVATIONS: DEREDDENED OPTICAL AND NEON SPECTRA ($I_{5007} = 1.000$)

					SNR 0540−69.3		
TRANSITION	CAS A[a]	G292.+1.8[b]	E102.2−7219[b]	N132D[b]	D&T84[b]	K89[c]	PUP A[d]
Estimated Reddening (c).....	2.06[e]	1.3[f]	0.04[g]	0.2[h]	0.2[h]	0.3	0.7
[O II] λλ7320+30.....	0.17	0.03	...	0.09	0.02	0.05	0.07
[O I] λ6300	0.04	0.02	0.03	0.10	0.03	0.05	0.06
[O III] λ5007.....	1.00	1.00	1.00	1.00	1.00	1.00	1.00
[O III] λ4959.....	0.26	0.33	0.34	0.34	0.30	...	0.28
[O III] λ4363.....	0.03	0.05	0.04	0.05	0.03	0.07	0.04
[Ne III] λ3869	0.30	0.16	0.14	0.10	...	0.02	0.16
[O II] λλ3727	0.58	2.12	1.34	2.39	0.63	0.39	1.69
[Ne V] λ3426	...	...	0.04	...	...	...	...
log (I_{7325}/I_{3727})	−0.54	−1.84	...	−1.44	−1.58	−0.86	−1.36
log (I_{5007}/I_{3727})	0.23	−0.33	−0.13	−0.38	0.20	0.40	−0.23
log (I_{3727}/I_{6300})	1.18	1.95	1.67	1.39	1.39	0.89	1.46
log (I_{4363}/I_{5007})	−1.52	−1.26	−1.36	−1.32	−1.46	−1.18	−1.35
log (I_{3426}/I_{3869})	...	...	−0.60	...	...	...	...

	PUP A[i]			N132D			G292.0+1.8
TRANSITION	Ω	O3	O4	7A	8A	11	GLOBAL
Estimated Reddening (c).....	0.7[d]	0.7[d]	0.7[d]	0.2[i]	0.2[i]	0.2[i]	1.3[f]
[O II] λλ7320+30.....	0.15	0.16	0.14	0.07	0.09	...	...
[O I] λ6300	0.10	...	...	0.01	0.04	0.04	0.03
[O III] λ5007.....	1.00	1.00	1.00	1.00	1.00	1.00	1.00
[O III] λ4959.....	0.35	0.36	0.35	0.38	0.35	0.33	0.35
[O III] λ4363.....	0.05	...	...	0.04	0.04	0.03	0.08
[Ne III] λ3869	0.19	...	...	0.14	0.05	0.08	0.26
[O II] λλ3727	2.03	0.93	2.87	1.94	2.03	1.66	3.54
[Ne V] λ3426	...	...	...	...	...	...	...
log (I_{7325}/I_{3727})	−1.13	−0.77	−1.32	−1.41	−1.33	...	...
log (I_{5007}/I_{3727})	−0.31	0.03	−0.46	−0.29	−0.31	−0.22	−0.55
log (I_{3727}/I_{6300})	1.32	...	...	2.13	1.67	1.57	2.10
log (I_{4363}/I_{5007})	−1.29	...	...	−1.38	−1.36	−1.55	−1.10
log (I_{3426}/I_{3869})	...	...	...	...	...	...	...

[a] Chevalier & Kirshner 1979.
[b] Dopita & Tuohy 1984.
[c] Kirshner et al. 1989.
[d] Winkler & Kirshner 1985.
[e] Chevalier & Kirshner 1979.
[f] Goss et al. 1979; Braun et al. 1986.
[g] Blair et al. 1989.
[h] Danzinger & Leibowitz 1985.
[i] Paper I.

these have been related approximately by

$$c \approx 1.44E(B-V) \approx 0.464A_v\,. \quad (1)$$

The reddening constants themselves have been collated from the literature and observations in Paper I.

3. THE BOW-SHOCK/CLOUD-SHOCK MODEL

The proposed model structure is that of an individual knot, or cloud, of oxygen-rich material which is traveling on the ballistic trajectory in a low-density medium. The cloud encounters a density discontinuity at a relative velocity of several thousand km s^{-1}. The discontinuity may be the reverse shock of the main SN blast wave, or some other local density contrast. The collision is highly supersonic in all the media. If a nominal density contrast of 1:100 is assumed between the ambient material and the cloud itself, cloud shocks of hundreds of km s^{-1} result.

The cloud in this model is classed as "small" by the criterion of McKee (1988), but not so small that the hydrodynamic treatment is invalid. A characteristic size of about 10^{17} cm has been taken on the basis of the long-term, collected works of Kamper & van den Bergh (1976) and van den Bergh & Kamper (1983, 1985) on Cas A, and Winkler et al. (1988) on Pup A, the two most spatially resolved remnants.

To permit a hydrodynamic treatment, the ballistic penetration of upstream ions should be small. The presence of a magnetic field B, results in a Larmor radius r_L for ions of mass m, velocity v, and charge Z of

$$r_L = vmc/(ZeB) \text{ cm}\,. \quad (2)$$

With a relatively small field of 1.0 μG, penetration of ions into the cloud is of the order $r_L = 3.1 \times 10^{12}$ cm for 5000 km s^{-1} O VIII ions, and less for lighter ions. This is much less than the 10^{17} cm clouds considered here, so that we may assume that ion penetration is not important, and bow-shock structures can form. The shock models in subsequent modeling include a 1.0 μG transverse magnetic field to remain consistent with this assumption.

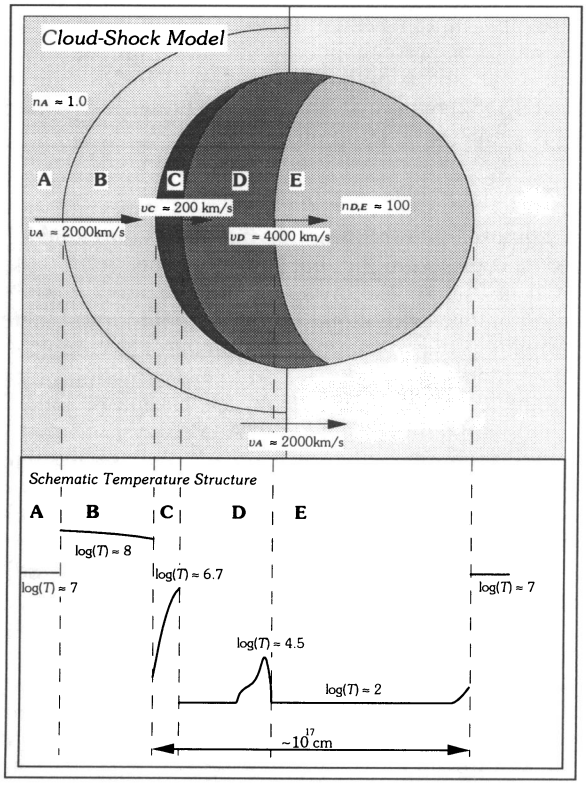

FIG. 1.—Schematic structure of the bow-shock/cloud-shock model. The cloud encounters a density contrast (A) (i.e., a reverse shock) at a relative velocity of several thousand km s^{-1}. The collision results in an approximately isobaric bow shock and internal shock structure (B and C), and a supersonic, isochoric ionization front (D) that precedes the internal shock into the cloud (E). The present simplified model is limited to these components, evolving over a cloud-crushing timescale. Other shock structures formed in the ablation and compression of the knot in the hydrodynamic crushing process are not considered.

The model structure is shown in schematic form in Figure 1. The present modeling assumes supersonic flow v_A of the ambient medium relative to the cloud, producing a stand-off bowshock (B). In such a bow-shock/cloud-shock model, a number of characteristic pressure ratios, velocities, and timescales are applicable and may be formulated following McKee & Cowie (1975).

When the March number of the collision is large, $M_A \geq 1$, the ratio of the ambient pressure and the pressure at the stagnation point, at the leading edge of the cloud, is given by

$$F = \frac{p_A}{p_C} = \left(\frac{\gamma+1}{2}\right)^{(\gamma+1)/(\gamma-1)} M_A^2 \left(\gamma - \frac{\gamma-1}{2M_A^2}\right), \quad (3)$$

where M_A is the Mach number of the shock at A, p_A and p_C are the pressures at A and C, and γ is the usual ratio of specific heats ($\gamma = 5/3$ for the monatomic plasmas here). An approximation for the pressure ratio is

$$F \approx 3.15 - 4.78x + 2.63x^2 , \quad (4)$$

where $x = v_C/v_A$. This is a maximum when the internal cloud shock is slow compared to the flow velocity into the bow shock. Equations (3) and (4) assume spherical geometry near the stagnation point.

The stagnation pressure at (B) drives a shock into the cloud (C), called the cloud shock, at a velocity v_C. In this structure, the dynamic ram pressure of A and C can be related approximately by

$$\rho_C v_C^2 \approx F \rho_A v_A^2 , \quad (5)$$

This expression may be used to make order-of-magnitude estimates of the cloud density ρ_C from the observed X-ray–emitting plasma pressure, if the X-ray pressure can be equated to p_A and the velocities can be assumed. In the model here, as opposed to main blast-wave–cloud interaction of the McKee & Cowie model description, the velocity of interaction is taken to be of the order of the cloud space velocity, as it collides with a standing discontinuity. The discontinuity is either another bow shock around a slow-moving dense cloud of normal composition, or else is the reverse shock of the main blast wave.

As seen above, the relationship between the cloud velocity and the internal shock velocity will be proportional to the square root of the cloud/medium density contrast, χ. The stagnation pressure ratio, F, will in practice be geometry dependent, and usually somewhat less than 3. In plane-parallel geometry $F = 1.0$, so that $v_A/v_C = \chi^{1/2}$. The modeling presented in the following sections assumes that if the range of cloud-shock velocities is 50–250 km s^{-1}, then the density contrast should be of order ≈ 100. Therefore, models with cloud number densities from 10 to 1000 cm^{-3} will be considered. With $\chi = 100$, this range is both consistent with the observed ambient densities in the range of 0.1–10 cm^{-1} (cf. Table 1) and will produce only minor line-quenching complications. Models outside this range are both difficult to model, and harder to justify observationally. The exceptional densities in the Cas A remnant shown in Table 1 suggest that these models may have difficulty matching the observed spectra of the Cas A knots.

For a cloud of radius a and a density contrast $\chi \gg 1$, the relevant timescales of the interaction are (McKee 1988)

$$\tau_c = \frac{a}{v_D} = \frac{\chi^{1/2} a}{v_A} \quad \text{(cloud-crushing time)} , \quad (6)$$

and

$$\tau_x = \frac{2a}{v_A} \quad \text{(cloud-crossing time)} . \quad (7)$$

With a typical knot velocity of 2000 km s^{-1} and knot dimensions of order 10^{17} cm, a crossing timescale is about 5×10^8 s. With χ between 10 and 100, a crushing timescale of ~ 1–2.5×10^9 s is appropriate. These timescales are small compared to the SNR evolution timescales (cf. Table 1). The recent three-dimensional numerical hydrodynamic of Stone & Norman (1992), with a density contrast of $\chi = 10$, lends support to this estimate of the crushing timescale and indicates that the cloud might expect to survive in a relatively complete state for about two crossing timescales (eq. [7]). Therefore, the value of order 10^9 s will be adopted as the hydrodynamic timescale. This is in very encouraging correspondence with the individual knot lifetime measurements for both the quasi-stationary flocculi (QSFs) and fast-moving knots in Cas A, by the combined efforts of Kamper & van den Burgh (1976; van den Burgh & Kamper 1983, 1985).

For the present work, the details of the cloud ablation, compression, and disruption are not taken into consideration in their effects on the spectral modeling, other than to place an upper limit on the timescale of the problem. The geometry is assumed to be constant up to the crushing time, and after 10^9 s the cloud is assumed to be dispersed and destroyed, termina-

ting the calculations. The simple shock and photoionization modeling here is based on a plane-parallel geometry. The ionization fronts travel at velocity v_D, which is supersonic in the cloud medium. This is therefore modeled as an isochoric, time-dependent photoionization problem, since the crossing, ionization heating, and cooling timescales are all much faster than the sound-crossing time.

The model of D87 assumed that nonradiative shocks (i.e., B in Fig. 1) in front of the cloud of oxygen-rich material produced the local X-ray field in the cloud which drove the ionization front. This locally generated field relieves the problem of trying to provide the intense field needed to drive an ionization front, using only the ambient radiation from the diffuse hot gas in the remnant as a whole (cf. Blair et al. 1989). The radiation from nonequilibrium models by Hamilton, Sarazin, & Chevalier (1983) was approximated by power-law radiation fields, with different spectral indices and cutoff frequencies. Furthermore, it was assumed that the ionizing field was constant throughout the evolution of the ionization front. This approximation means that the field generated by the shocks must turn on, and become steady, very rapidly compared to the evolution timescale of the ionization front.

The model of D87 used an "instant illumination" approximation, where the full radiation field was applied from the start. Here, the new, extended, MAPPINGS II code can consistently model both the shock emission and the ionization from models within the one-model framework, and this approximation can be tested by studying the emission evolution of the shocks in detail. This allows us to achieve a much greater degree of self-consistency. The modeling code, MAPPINGS II, used here, is described in more detail in Sutherland & Dopita (1993) and Sutherland (1993). It has accommodation for up to 16 atoms, although only a subset will be used here. All stages of ionization are allowed for.

The initial set of abundances for the preliminary models used to determine the parameters of the cloud collision model are given in Table 3. These abundances are loosely based on the oxygen-neon layers from the 25 $M_\odot$ evolutionary and explosive models of Weaver, Zimmerman, & Woosley (1978), Woosley, Axelrod, & Weaver (1984), and Johnston & Yahil (1984) and were measured manually from the plots of the composition structure.

The observations presented here of N132D, Pup A, and SNR G292.0+1.8 consistently failed to display any sulfur emission, so a set is used that does not include a contribution from the deepest heavy elements, using only carbon, oxygen, neon, magnesium, and silicon. This composition is probably applicable to the majority of the remnants, except SNR 0540−69.3 and some knots in Cas A.

TABLE 3

INITIAL ABUNDANCES

Element	Abundance
H	−6.00
He	−6.00
C	−1.05
O	0.00
Ne	−0.34
Mg	−1.34
Si	−2.72

NOTE.—Log numbers relative to O = 0.00.

The hydrogen and helium abundances are set to insignificant levels, but were explicitly included in the modeling because some aspects of the original MAPPINGS code design (cf. Binette 1982) require at least a token presence of these ions. Their presence had no effect on the models.

4. SHOCK MODELS

It is proposed that the radiation that drives the cloud ionization fronts comes from the shock waves in the model structure (A and B in Fig. 1). The evolution of these shocks, especially the slower, oxygen-rich cloud shock, is an important factor in the feasibility of the ionization front model. The complete self-consistent time-dependent solution to the evolution of such a shock wave entering a neutral oxygen plasma presents considerable computational difficulty. Accordingly, a number of simplifying assumptions have been made and are presented in the following sections.

The bow shock is formed by material from the ambient SNR medium and is likely to be composed of the fairly normal composition material detected in X-ray observations (i.e., Clark et al. 1982). In contrast, the cloud shock is in the oxygen-rich material that gives rise to the unusual optical emission that characterizes the OSNRs. Shocks that form in such plasmas are extreme in many ways. The high molecular weight of these super–metal-rich plasmas results in high postshock temperatures. This is apparent from the relationship between the temperature jump (T_s), the shock velocity (v), and the mean molecular weight (μ), where $T_s = 3\mu v^2/16k$ K. Thus, a shock moving into atomic oxygen at 200 km s^{-1} may achieve $\sim 1.5 \times 10^7$ K. In practice, the preshock plasma is often fairly highly preionized and ratios of 5 or more electrons per ion are common. This has a strong effect on the mean molecular weight (μ), and hence the preionization has a strong effect on the shock thermal structure. This is in contrast to normal composition shocks where the electron-to-ion ratio is always around 1.2 once ionization has occurred. To simplify the subsequent calculations, a steady preionization will be assumed for the shock-wave models. It remains to be shown that the preionization can be set up on a rapid enough timescale that this assumption has some validity.

Finally, due to the simplified radiative transfer treatment used, we require a steady ionizing source. To meet this requirement, it needs to be shown that, with some reasonable parameters, shocks can form rapidly and become radiative in a timescale short compared to the cloud-crushing timescale τ_c (eq. [6]). This implies both a rapid cooling timescale and a steady preionization of the gas entering the shock so that the thermal structure is constant.

4.1. *Thermal Stability of Oxygen-rich Shocks*

The question arises of the stability of the shocks involved in the present oxygen-rich models. Without a hydrodynamic code with radiative cooling, it is difficult to predict the detailed stability properties of these oxygen-neon mixtures. The criterion of Schwartz, McCray, & Stein (1972),

$$\frac{d\ln(\Lambda_N)}{d\ln(T)} > 2\,, \tag{8}$$

is not strictly satisfied by the oxygen-rich cooling functions, shown by the curves in Figure 2. Nevertheless, while the overall cooling rates are many orders of magnitude greater than typical cosmic abundance cooling curves, the slopes of the

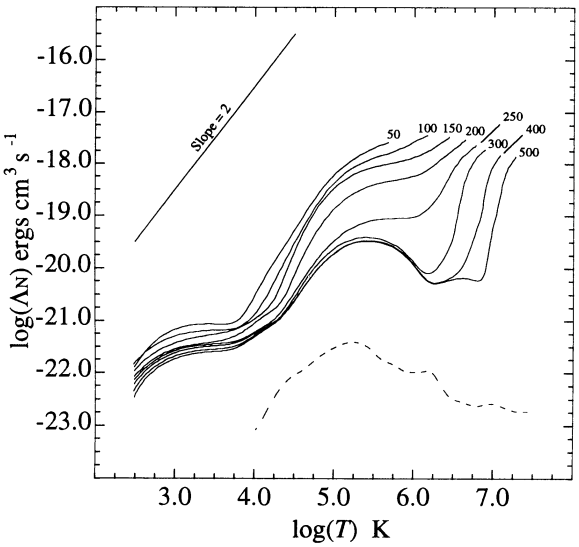

FIG. 2.—Cooling functions of oxygen-rich self-consistent shock models with velocities of 50–500 km s^{-1}. Below 300 km s^{-1} the curves are monotonically decreasing, and it is likely that the shocks will be thermally stable. The 300, 400, and 500 km s^{-1} models may not be stable. A full-field nonequilibrium curve from Sutherland & Dopita (1993) for log $T_0 = 7.5$ is shown on the same scale by the dashed line.

cooling functions are at least monotonically decreasing, and the slopes are as great as two in some regions, with an average slope of about unity. The slopes are comparable to the slope of the nonequilibrium cooling function below 10^5 K of Sutherland & Dopita (1993), shown as a dashed curve, which corresponds to the range of temperatures reached in stable normal composition shock models. A line of slope two is included on the plot for comparison. The plot suggests that the oxygen-rich shocks are probably thermally stable up to 250 km s^{-1}. Above 250 km s^{-1}, the 300–500 km s^{-1} models show regions of negative slope and are thermally unstable.

Fortunately, the stability or otherwise of the ionizing shocks may turn out to be unimportant to the emitted optical spectra. In normal cosmic abundance, radiative shock models, the cooled recombination zone is several thousand degrees, and the optical emission is strongly affected by photoionization due to the downstream field of the shock. The [O I], [S II], and other low-ionization emission lines are particularly affected and hence are sensitive to the radiative transfer effects resulting from any shock flow instability. In the oxygen-rich case, the cooled recombined zone is so cold that no collisional emission occurs, even in the full diffuse field models. Thus the downstream radiative transfer has little effect on the emitted spectrum. Since instabilities will form on a cooling timescale, the hotter emitting regions will not be affected either. In this sense then, the instability of the shocks will not greatly affect the ionizing radiation, or the optical spectra of the models.

One effect of the shock stability that may still be important is the transfer of the bow-shock radiation which will have to penetrate the cloud shock to reach the interior of the cloud and any ionization fronts. If the cloud shock is unstable, or otherwise disrupted, then the hard bow-shock radiation can reach the interior. Whether this is important or not will be determined in the subsequent bow-shock and photoionization modeling. If significant, the bow-shock spectrum can simply be added to the ionizing source vectors.

The ionizing radiation field of the cloud shock will be calculated with normal, smooth shock models which are terminated at a temperature of 300 K, defining the cooling length in these models.

4.2. *The Cloud Shock*

Cloud-shock models were computed with a preshock density of 10–1000 cm^{-3} and a velocity range of 50–500 km s^{-1}. A transverse magnetic field of 1.0 μG was assumed for all models. A self-consistent equilibrium preionization of the precursor gas entering the shock front was assumed. The oxygen-neon abundance mixture used is that of Table 3.

The model structure and its properties are summarized in Table 4. The cooling timescales and lengths are given in a normalized form, since they scale as the inverse of the plasma density over the density range considered. This table shows that, for shock velocities less than 300 km s^{-1} (models OS050–OS250), the cooling timescale will be short compared to the cloud-crushing time of 10^9 s, even with the lowest density of 10 cm^{-3}. If the faster shock velocities must be used (models OS300, OS400, and OS500), then the density would have to be increased to 100 cm^{-3} or more, to shorten the cooling timescales. The upstream ionization parameter (Q, defined below) is very great. All the models, even the 50 km s^{-1} OS050 model, are capable of producing significant preionization.

The thermal and ionization structure of the 200 km s^{-1} shock is shown in Figure 3. This figure clearly demonstrates the unusual features of the oxygen-rich shock models. The initial ionization is very rapid, due to the large number of free electrons entering the shock, and the cooling is similarly rapid. Once ionized, the highly ionized species like O V and O VI remain at virtually constant levels throughout the model, down to 300 K, due to their slow recombination rates. By the time the plasma has cooled, it is still dominated by O III and O V. The [O I] emission is very weak, and the [O II] lines are considerably weaker than the [O III] lines in the final spectrum, in contrast to models of normal composition material. The suppression of the [O II] and [O I] emission, caused by the very low temperature in the recombination zone, is the main reason that simple radiative shock models fail to reproduce the observed spectra.

4.3. *Preionization*

The degree of plasma preionization critically affects the molecular weight, and hence the shock jump conditions. Even one ionization per atom effectively halves the molecular weight of plasma, and hence the shock temperature. To determine the extent of the effects of the preionization, limiting cases are considered. Test models were run where the gas entering a 200 km s^{-1} shock was held to be artificially neutral or singly or

TABLE 4

OXYGEN-RICH SHOCK MODELS

Model	$\log(v_s)$ (cm s^{-1})	$\log(T_s)$ (K)	$\log(d_3 n_0)$ (cm^{-2})	$\log(\tau_3 n_0)$ (s cm^{-3})	$\log(Q)$ (cm s^{-1})
OS050	6.70	5.68	12.93	7.47	7.27
OS075	6.88	5.96	13.18	7.40	7.76
OS100	7.00	6.16	13.45	7.48	8.17
OS150	7.18	6.44	13.93	7.67	8.61
OS200	7.30	6.64	14.38	7.99	8.93
OS250	7.40	6.77	15.00	8.58	9.33
OS300	7.48	6.89	16.09	9.62	9.49
OS400	7.60	7.08	17.69	10.08	9.65
OS500	7.70	7.27	17.23	10.45	9.70

NOTE.—n_0 = precursor oxygen atoms per cm^3.

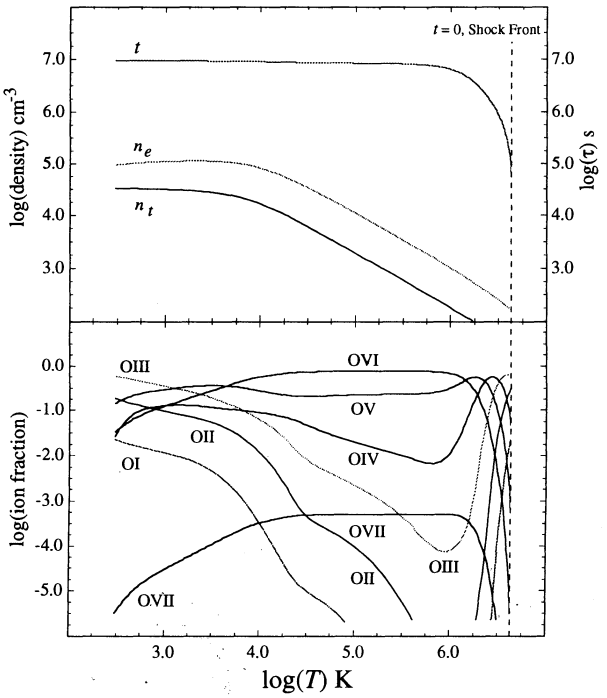

FIG. 3.—Thermal structure of the 200 km s^{-1} cloud shock. The lower panel shows the oxygen ionization structure for the model. The principal variable used here is T, the temperature. This allows the structure to be resolved in the plots, whereas if a time or distance coordinate were used, the structure changes would be too spatially rapid to be clearly seen. The flow time variable is shown as a function of temperature, showing how most time is spent at a high temperature followed by very rapid cooling.

fully self-consistently ionized, to measure limits on the build-up of the upstream radiation field, and thence the timescales over which preionization may occur.

The shock without preionization has a much higher temperature initially, but the lack of electrons limits the emission process. In the models with preionization, the initial temperature is lower, a factor that is compensated by the immediate availability of electrons. The question of how soon the field can build up in the precursor zone will then be a matter of the competing factors of electron availability and the range of electron energies.

The radiation field build-up is given in Figure 4, where the potential ionization front velocity is plotted as a function of the shock development. The ionization front velocity is approximated by

$$v_f = \frac{Q}{\overline{N_i}} \text{ cm s}^{-1}, \quad (9)$$

where v_f is the nominal front velocity, $\overline{N_i}$ is the mean number of ionizations per particle, and Q is the ionizing photon flux per particle density (cm s^{-1}). The velocity estimates in the test sequence used $\overline{N_i} = 2.54$ stages per ion, as achieved in the steady-flow equilibrium preionization model; thus the velocities will be underestimates of the spread of the early ionization fronts when less ionization has occurred. The model thermal structures are given in Figure 5, and the effect on the shock temperature can be seen clearly.

The radiation build-up timescale, to the point where an ionization front velocity could exceed the shock velocity, is very short. This result holds irrespective of the actual preionization

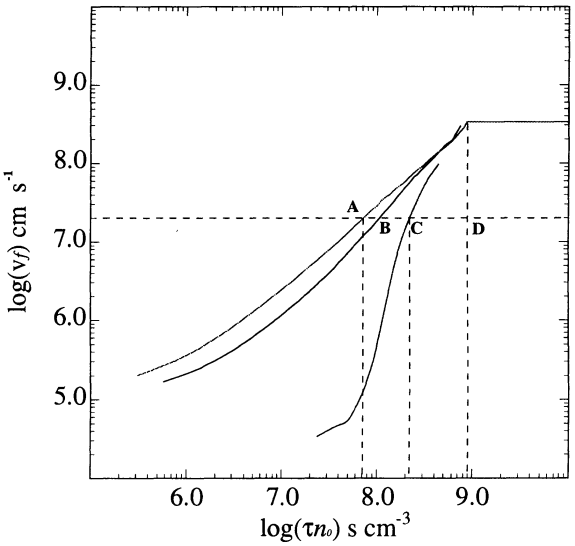

FIG. 4.—Preionization timescales. The times required to generate an ionization front that travels faster than the generating 200 km s^{-1} shock. The curves represent initial front velocities for artificially neutral (A), singly (B), and fully (C) preionized shock models. Once the curves exceed 2×10^7 cm s^{-1}, preionization can occur. The field build-up is very rapid, irrespective of the preionization.

state in the precursor material. The model where the precursor is held artificially neutral provides an upper limit and gives a value of 2×10^8 s cm^{-3}, or $\sim$20 times the cooling timescales of the model. The limiting factor is the electron availability, causing the neutral model (A in Fig. 5) to lag until some ionization has occurred. At this point the ionizing flux effectively switches on to nearly full power. This timescale, along with the overall shock-cooling timescale, will scale inversely with density, so that the ionization front will always form on a timescale that is rapid compared with the other cloud timescales, at all reasonable cloud densities.

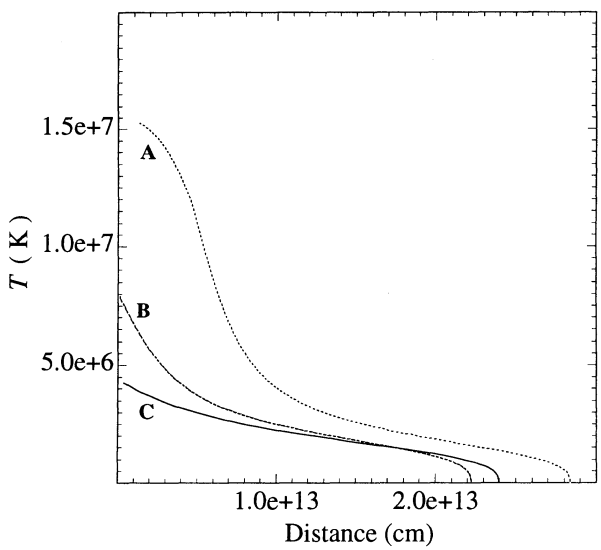

FIG. 5.—Preionization thermal structures. The effect of the preionization on the shock thermal structures may be seen here. The models labeled A, B, and C correspond to the curves of the same labels in Fig. 4. The oxygen-rich composition models are particularly sensitive to the preionization.

This result allows the simplification that the shock is traveling into a full equilibrium preionization balance determined for each shock velocity. The preionization is limited only by the response time of the ionizing plasma in the precursor zone, and not by the build-up timescale of the ionizing radiation. Once a complete ionization front structure is established, the shock structure, and hence the exciting radiation source, will be steady. It merely remains to show that the ionization front structures can complete, producing equilibrium ionization, well within the cloud-crushing timescale. This will permit the formation of the steady state model where the ionization front has completely detached from the shock front, allowing the two components to be calculated independently.

4.4. *Radiation from the Bow Shock*

The very fast bow-shock structure may be an important X-ray ionizing source, in addition to any internal cloud shocks. In the present model, the cloud is assumed to be encountering the reverse shock reflected from behind the main SN blast wave as it sweeps up interstellar material and begins to slow down. There is some evidence for such a structure in the Cas A remnant in radio observations of Fabian et al. (1980). In the case of N132D, the SNR may be expanding into a low-density cavity, and the evolutionary status of the main reverse shock is uncertain. In that remnant there is some evidence that the oxygen-rich material is spatially associated with the remains of some dense circumstellar material of more normal composition (cf. Paper I). In this case, the encounter may be between the oxygen-rich cloud and a reflected shock from the slow-moving material, or the slow-moving material itself.

To determine the importance of the bow shock to the total radiation field in the ionization front modeling, fast shock models have been constructed. A bow-shock spectrum for a 2000 km s^{-1} plane-parallel shock was evolved for a length of 10^{17} cm. The length was estimated for the typical standoff distance of a bow shock of about one cloud diameter, guided by the three-dimensional models of Stone & Norman (1992). This should be good to an order of magnitude. The preionization was estimated for a 10^7 K plasma in collisional equilibrium at a density of 0.1 cm^{-3}, in broad agreement with the observed global X-ray spectra of the remnants (Table 1), at the density implied by a 100:1 density contrast. The composition was taken to be normal cosmic abundances in one model, and a comparison model of oxygen-rich composition was also made.

In both models, cooling over this length is negligible, $\Delta T \ll 1\%$. The shock jump conditions predict a postshock temperature of 1.8×10^8 K in the oxygen-rich material, near the upper limits of the modeling code, and of 6.5×10^7 K for the normal material. The difference between these is not very great because the very large number of free electrons in the oxygen-rich plasma greatly reduce the mean molecular weight. As the precursor gas entering the bow shock is already highly collisionally ionized, photoionization precursors do not exist for these models.

The bow-shock model is truncated at 10^{17} cm, on a timescale that is very short compared to other timescales in the shock models, and the emitted spectrum is produced essentially by a homogeneous slab of underionized hot plasma, which grows linearly with time for a cloud-crossing time and would then remain roughly constant until the cloud is destroyed in another crossing time. The two spectra, from the normal and oxygen-rich models, are therefore very similar in shape, but the intensity of the oxygen-rich model is very much greater than that of the normal composition model. The flux incident on the cloud itself, in terms of the ionization parameter, Q, is 1.9×10^{10} cm^{-2} s^{-1} for the oxygen-rich model, and only 2.8×10^6 cm^2 s^{-1} for the normal model. The ionizing bow-shock spectra are shown in Figure 6 along with the cloud-shock spectra.

The case where the bow shock occurs in oxygen-rich material presents a serious difficulty for the subsequent modeling, as it generates a photon source that is very strong compared to those generated by the cloud shocks and is capable of modifying both the cloud shock and the ionization front. The intensity will increase linearly throughout the evolution of the cloud shock and its ionization front. The radiative transfer problem this presents may not be modeled with the present code. However, the X-ray observations of the OSNR suggest that this type of oxygen-rich bow shock probably does not occur. The surface brightness of such a bow shock, of order 100 ergs cm^{-2} s^{-1} over an area of $\sim \pi a^2 \approx 3 \times 10^{34}$ cm^2 would imply that a *single* knot would provide $\sim 3 \times 10^{36}$ ergs s^{-1}, or roughly the total measured X-ray luminosity of Cas A (see Table 1). This is *not* observed. For this reason, the normal composition bow shock has been chosen. In this case, the ionization parameter is much lower than the cloud-shock emission by a factor of 10–100, a factor that would be further reduced by geometrical dilution, so it has therefore been neglected in the subsequent modeling.

This indication that the intercloud medium has a normal composition, whereas the clouds are oxygen-rich, clearly is an important constraint of theoretical models of the stellar explosion itself.

5. R-TYPE IONIZATION FRONT MODELS

At an ionization front, an incident photon radiation field is absorbed in a thin layer. The velocity is limited by the ratio of the number of available photons and the number of absorbing particles. When the particles can be multiply ionized, as in the oxygen-rich plasmas the effective number of absorbing particles, N_i, is increased and the ionization front velocity is slower (eq. [9]). The theory of ionization fronts is due to Kahn (1954), Goldsworthy (1961), and Axford (1961). This area was further expanded on by Mendis (1968a, b, 1969). In the nomenclature developed by those authors, the current ionization front models represent weak R-type ionization fronts.

In order to approximate this situation within the framework of the present modeling code, the procedure of D87 is adopted. The improvement afforded by the new developments of MAPPINGS II lies in the detailed shock models of the previous section. The photoionization model computed here benefits from more recent atomic data and a broader ionization range, but otherwise the models are very similar.

5.1. *Ionization Front Model Structure*

The ionization front model consists of a thin slab of plasma that is subject to the radiation field of the shocks calculated previously. The radiation field is assumed to be not attenuated by material between the front and the shock. This assumption is justified as long as the distance remains significantly shorter than the Strömgren column of the ionizing radiation. For the present modeling of a 10^{17} cloud, this optically thin assumption will place an upper limit on the cloud density that may be modeled. This limit is determined in § 6.

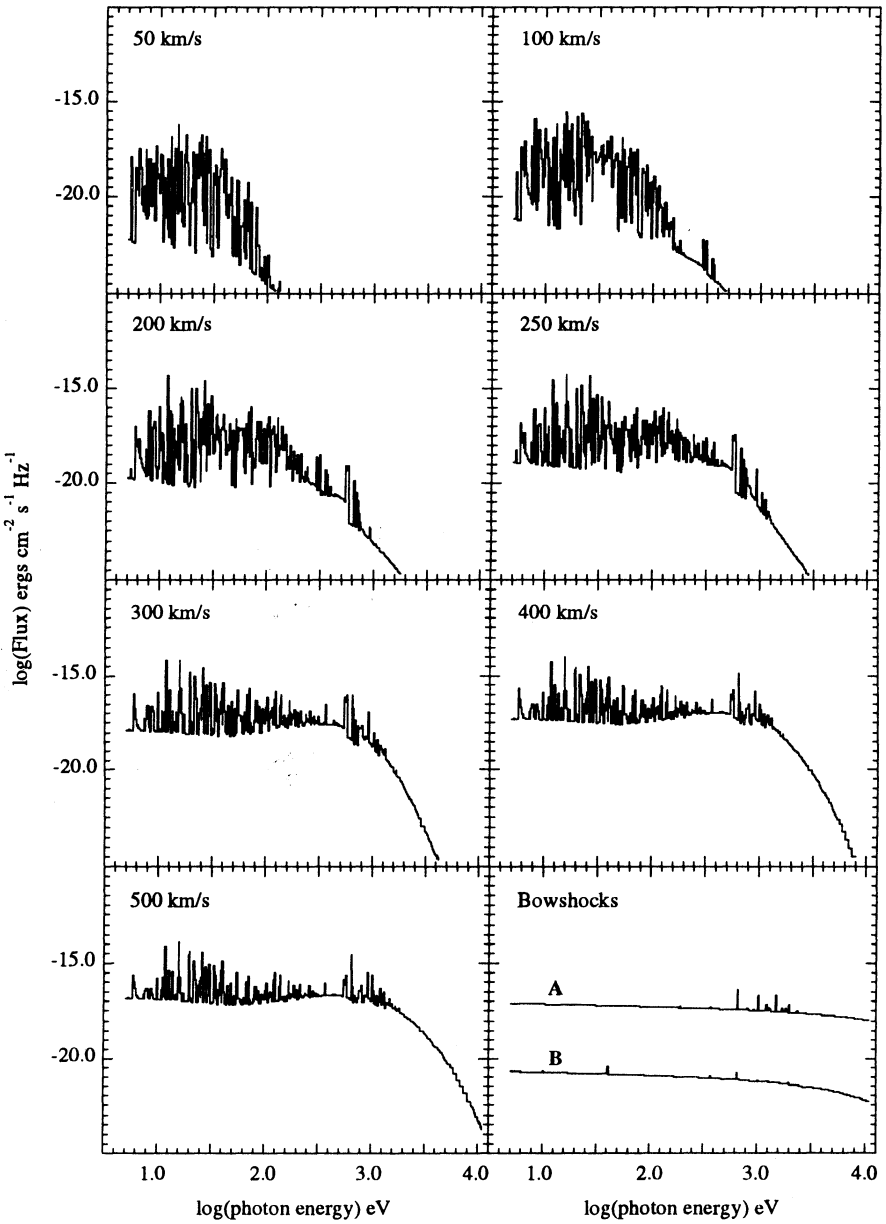

FIG. 6.—Ionizing radiation. The radiation fields of the cloud-shock models and the bow-shock models are shown. These form the sources for the subsequent ionization front models.

The most serious restriction of the model is that the slab element is assumed to be optically thin. In this sense, the results calculated are the response of a volume element to the total incident field, but the internal absorption across a real ionization front is not taken into account. This approximation will produce a higher average ionization in the models than in reality. These ionization front models are analogous to the Lagrangian shock flow models, where a single parcel of material is followed through the shock structure and the final spectrum of the whole is the averaged sum of emission of the parcel traveling through the structure. The ionization front spectrum is taken as the time-weighted sum of the slab element over the course of the model evolution.

As an alternative to setting up a large grid of points and solving the radiative transfer differential equations simultaneously, this method provides a very easy approximation. The deficiencies will lie in the computation of the emission from the low-ionization species, such as O I, which may be underestimated. The calculation of the more highly ionized stages should be a more reasonable approximation, since these species will occur in the optically thin regions of the ionizing front. In addition, the heating effect of the radiation field will be overestimated, and an actual front may not reach the high temperatures achieved here.

The thermal structure of an oxygen-rich ionization front is shown schematically in Figure 7. The parameters used to describe the ionization front models in subsequent sections are shown on the diagram. The peak temperature is denoted T_p. The timescale to reach this peak is τ_p, and in those models that achieve a cold equilibrium, a cooling timescale τ_3 is also

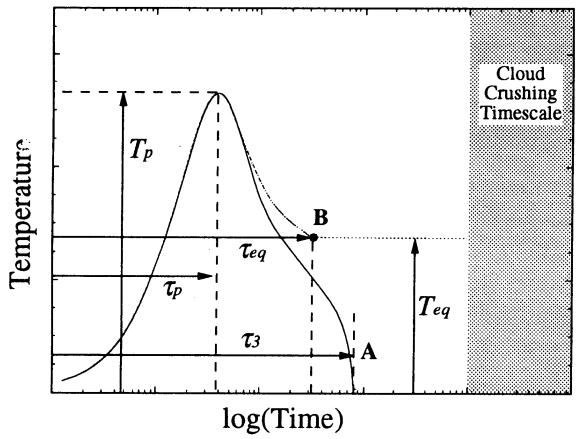

FIG. 7.—Thermal structure of an ionization front model. The parameters τ_3, τ_p, T_p, and τ_{eq} used to describe the front models are shown.

defined. Integration of the emission over this time defines the long-term steady emission of the front structure. Some of the faster ionization fronts result in such strong ionization that the efficient coolants such as O III, C IV, and O IV are depleted and cooling is reduced to the point where a hot equilibrium becomes possible, The integrated spectrum of these models is a continuing function of time, and no τ_3 exists. A general equilibrium timescale τ_{eq} is defined, in these cases, by the time required to reach thermal photoionization equilibrium.

The ionization front models (OP050–OP500) for the range of shock velocities considered in § 4 displayed the thermal structures shown in Figure 8. The models are also summarized in Table 5.

Generally the front models achieve quite high temperatures. However, the OP050 model (the 50 km s^{-1} shock source) only barely achieves 10^4 K, and as the radiation flux should vary as v^3, this model represents the lower limit of cloud-shock velocities that will produce this type of ionization front structure.

In one group of models, for shock velocities of 250 km s^{-1} or less, the temperature rises and then falls to a very cold state, which is nevertheless highly ionized. For these cold models, τ_3 is clearly defined. The equilibrium timescale τ_{eq} in these models is essentially the same as the cooling timescale. The second group of models (OP300, OP400, and OP500) stays hot, as the plasma becomes so ionized that the efficient coolants of O III and O IV are only present in small amounts. For these models only the equilibrium timescale, τ_{eq}, is appropriate.

TABLE 5

OXYGEN-RICH PRECURSOR MODELS

Model	N_i (cm^{-3})	log(v_f) (cm s^{-1})	log(T_p) (K)	log($\tau_p n$) (s cm^{-3})	log($\tau_3 n$) (s cm^{-3})	log($\tau_{eq} n$) (s cm^{-3})
OP050	1.04	7.26	3.94	9.44	10.17	...
OP075	1.42	7.61	4.09	8.98	9.83	...
OP100	1.69	7.94	4.15	8.68	9.73	...
OP150	2.25	8.26	4.33	8.35	9.77	...
OP200	2.54	8.52	4.43	8.09	9.84	...
OP250	3.02	8.85	4.47	7.97	10.08	...
OP300	3.80	8.91	4.56	7.91	...	9.62
OP400	4.56	8.99	4.69	7.81	...	10.08
OP500	5.03	9.00	4.77	7.74	...	10.45

NOTE.—n = oxygen atoms per cm^3.

The ionization structure of the OP200 model is shown in Figure 9. This shows the rapid ionization, and eventual equilibrium in a highly ionized state, when the temperature is much less than 1000 K, as can be seen by comparison with Figure 8. This figure agrees in general with Figure 2 of D87.

5.2. *General Features of Ionization Front Spectra*

The detailed integrated spectra of the ionization front models are discussed in § 7, when the final models are presented.

The time-dependent optical emission of the model OP200 (200 km s^{-1} shock) is shown in Figure 10. The timescale here is normalized to density. The figure shows the integrated emission of the optical forbidden oxygen lines of O I, O II, and O III, normalized to [O III] λ5007 = 1.00, as a function of time, as the gas element traverses the ionization front. The spectrum is dominated initially by [O I] λ6300, and then [O II] $\lambda\lambda$3727 and [O III] λ5007 together become the main emission. In this model the final [O II] $\lambda\lambda$3727 and [O III] λ5007 lines are of comparable intensity, the [O II] lines being slightly brighter (as

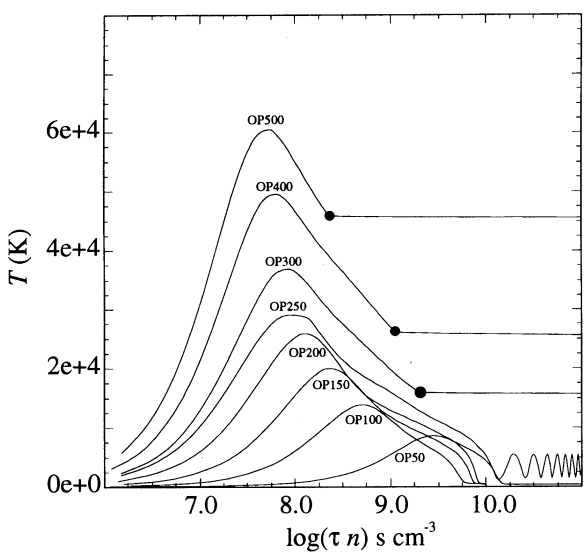

FIG. 8.—Thermal structure of the ionization front models

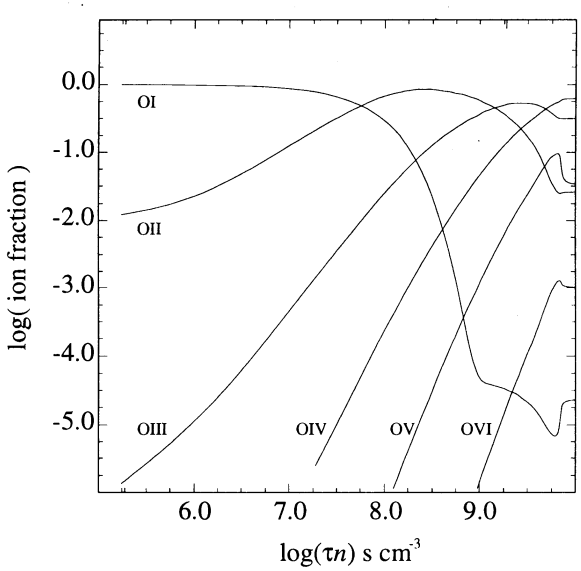

FIG. 9.—Oxygen ionization structure of the OP200 ionization front model

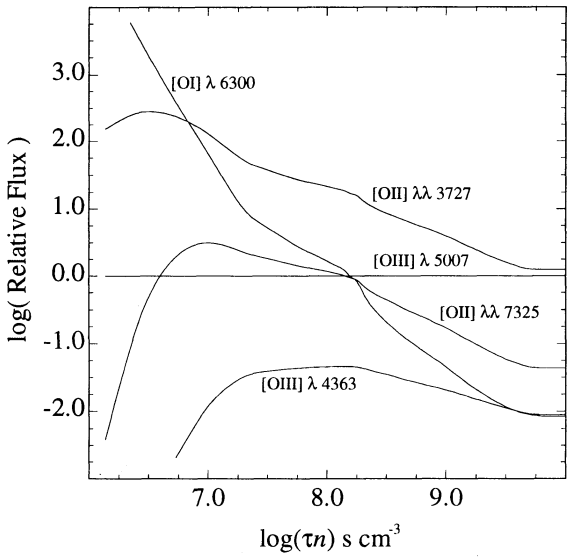

FIG. 10.—Time dependence of the OP200 ionization front model optical oxygen emission.

observed). The [O I] λ6300 line diminishes until it is reduced to about 1 times [O III] λ5007 and is comparable to the [O III] λ4363 line. This is one of the distinguishing features of these ionization front models, which produce much more [O I] emission than any equilibrium models with the same radiation fields, even though the [O I] emission may still be underestimated in these models. The [O III] λ4363 line rises rapidly with the temperature and peaks with the temperature peak before slowly dropping to about 1 times [O III] λ5007. This final value is somewhat low compared to the observed ratio of 2–8 (cf. Table 2). It must be stressed that this figure represents the ionization front emission in isolation and does not include the important contribution from the shock emission. As will be seen, the shocks contribute strongly to the [O III] emission and little to the [O I] and [O II] emission.

5.3. *Ionization Front Summary*

The present ionization front model thermal structures display the high temperature peaks, predicted by D87. The peak temperatures achieved in these models are higher, alleviating the need for separate electron and ion temperatures suggested in the earlier work as a means of increasing the excitation temperature.

It has been shown that the cloud-shock models can drive rapid ionization fronts that will precede the cloud shock. Provided that the bow shock of the cloud occurs in normal composition material, the radiation field due to the bow shock has been shown to be overwhelmed by the cloud shock emission. The cloud shocks may be thermally stable and optically thick to any bow-shock radiation. This represents a departure from the original D87 model, and it arises because the bow shock can only radiate a small fraction of the incident energy flux during the time available, while the cloud shock is fully radiative and highly efficient at converting mechanical energy into ionizing radiation.

The ionization fronts can achieve photoionization equilibrium (either cold or hot) in a short timescale given a high enough density, justifying the equilibrium preionization assumption used in the shock modeling. The final modeling will have to balance the inverse density effects on the front evolution timescale, to meet the requirement of shock preionization, with the direct density effect on the total cloud optical depth.

For the present work, the models are separated into the cold and hot equilibrium models. Detailed modeling of the hot equilibrium models is deferred to possible future work. This is due mainly to the problem presented by the continuing integration of the hot models throughout the cloud-crushing timescale. Cloud crushing will affect the radiative transfer in the models throughout the emission evolution, and the simple plane-parallel formalism is inadequate. On this basis, then, we proceed to the final model selection, taking models OP050–OP250 as being appropriate to the present modeling technique.

6. SELECTION OF MODEL PARAMETERS

Given the properties of the shock and ionization front models in the preceding sections, it remains to select a set of modeling parameters with which the models retain a degree of validity. The problem here is not to determine the conditions that need to be modeled, but rather to choose the conditions that *may* be modeled.

The structure envisaged is of a steady-flow, nonequilibrium model, where the cloud-shock structure is fully radiative and where the ionization front has detached and is traversing the main body of the cloud. This is depicted in Figure 1 in the lower panel. This detached, steady state is necessary if the preionization assumptions of the shock modeling are to be satisfied. By requiring that the front be detached and fully evolved, the Lagrangian modeling procedure of integrating the emission of a small "parcel" of material as it traverses the structure may be used. This method cannot be used for early stages of the evolution, where the shock and front structure are closely coupled, or when the front evolves slowly compared to the hydrodynamic evolution of the cloud.

The selection of model parameters will be made on the basis of the model structure results of the previous sections, in combination with the characteristic timescales of the problem as outlined in § 3. The main selection criteria will be to remain within the limitations of the present simplified modeling procedure as well as remaining within physically reasonable limits. The final models will *not* be selected on the basis of the detailed fit to the observed spectra.

6.1. *Characteristic Timescales*

The cloud-crushing timescale, τ_c (eq. [6]), is the fundamental timescale in the problem. The other characteristic timescales, those of the front evolution, τ_3 (cf. Fig. 7), and shock cooling, τ_{cool}, will determine a range of parameters where the modeling is valid.

For a given composition (Table 3), we need to choose a range of velocities and densities where the front evolves much faster than the cloud-crushing timescale and the shock evolves much more rapidly than the ionization front. Therefore, we require that τ_c is more than about 3 times τ_3, which is in turn more than 3 times τ_{cool}. This gives each structure, both ionization front and cloud shock, ample time to form and achieve a steady state within the overall problem timescale. Figure 11 plots the normalized timescales τ_3/τ_c (or τ_{eq}/τ_c) for the ionization fronts against the normalized cooling timescale τ_{cool}/τ_c for the shock models. The curves are plotted for cloud densities of 10 and 100 cm^{-3}. The faster shock models (300–500 km s^{-1})

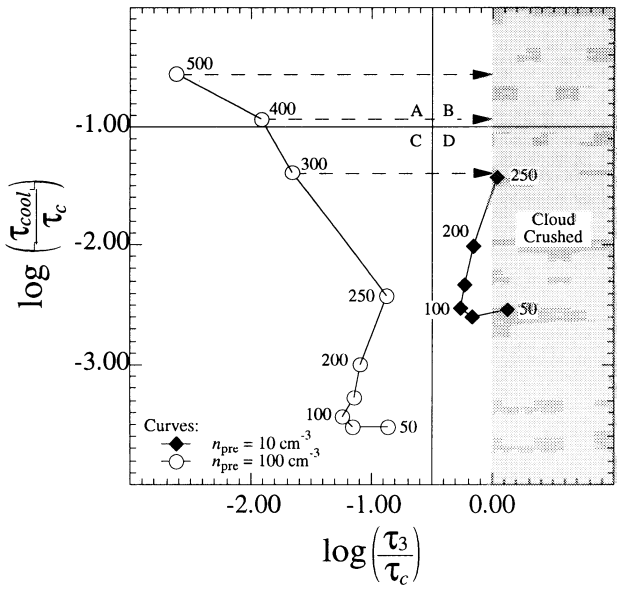

FIG. 11.—Characteristic timescales. The photoionization (τ_3) and shock (τ_{cool}) timescales are compared with the cloud-crushing timescale. Models that fall in quadrant C satisfy the modeling restrictions. See text for details.

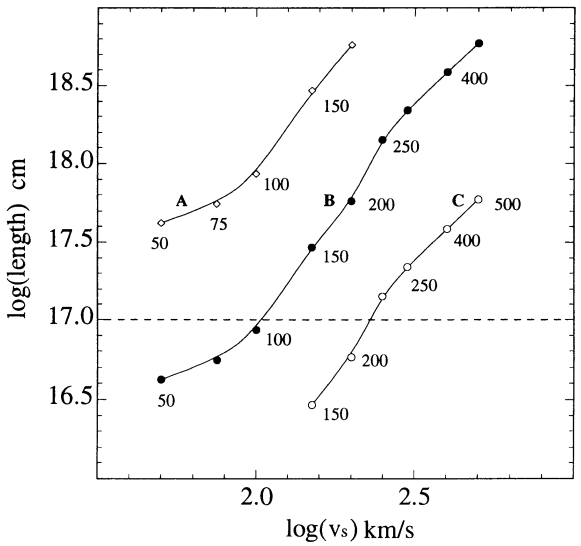

FIG. 12.—Cloud optical depths. The middle curve (B) shows the estimated length of an optical depth of the oxygen-rich material to the ionizing fields for model densities of 100 cm^{-3}. The outer curves represent 10 (A) and 1000 (C) cm^{-3} densities. Only the models larger than, or similar to, the cloud length (*dashed line*) have validity.

have been included for comparison, although they have already been eliminated from the range of validity in the previous sections. These fast shock models produce a hot precursor photoionization equilibrium, and the integrated spectrum will continue to grow throughout the cloud crushing time. This is indicated by the dashed horizontal lines.

The figure is divided into four quadrants, A. B. C. and D. Points that fall within quadrant A are models where the shock structure evolves slowly compared to the crushing time of the cloud. This makes the radiation source variable throughout the emission process, thereby invalidating the modeling procedure adopted here. Quadrant B contains models where both the shock and ionization models evolve too slowly. In quadrant D the ionization front models evolve too slowly. Finally, the points that fall within quadrant C represent models where the ionization fronts have time to form and evolve much more quickly than the dynamic lifetime of the cloud. At the same time, the shock models evolve more quickly still, reaching a steady emission state very rapidly, thus allowing the steady source approximation. As can be seen, the models with a cloud density of 10 cm^{-3} fall in quadrant D and cannot be modeled with the present methods, although this density regime is of course not excluded in actual clouds. Some of the 100 cm^{-3} models fall in the desired quadrant A. From this diagram, it is clear that if these models are to be used, then the cloud density must be 100 cm^{-3} or greater.

6.2. *Cloud Optical Depth*

Another limitation in the modeling lies in the steady, constant-source approximation of the ionization fronts. This requires that the material between the hot ionization front and the source, the cloud shock, remains optically thin. The Strömgren length for the shock radiation to be absorbed in a plane-parallel geometry has been modeled explicitly for $n_0 = 100$ cm^{-3}, and the results for the radiation from the range of shock velocities are shown in Figure 12. Scaled curves for 10, 100, and 1000 cm^{-3} are also shown. All the models remain optically thin in the low-density, 10 cm^{-3}, case, marginally thin in the 100 cm^{-3} case, and largely optically thick in the 1000 cm^{-3} case. For this reason, the final models will be made with a cloud density of 100 cm^{-3}. This density is happily consistent with the observations. From Table 1, it is apparent that, except for Cas A, the hot X-ray–emitting plasma has a density in the range 0.1–10 cm^{-3}. By taking a cloud density of 100 cm^{-3}, a reasonable density contrast of $\chi \approx 100$ is achieved. This type of density contrast also lends validity to the hydrodynamic arguments in § 3.

7. FINAL MODELS

Models were constructed from the shock models OS050–OS250 and the corresponding ionization front models OP050–OP250, scaled to a preshock density of 100 cm^{-3}. The spectra of the shocks and the ionization front models were integrated and co-added. First, the isolated optical shock spectra are compared with the observations, and then the combined models (designated OSP050–OSP250) are compared. In addition, the UV spectra are compared with the UV observations of Blair et al. (1989) of the remnant SNR E102.2 – 7219.

7.1. *Shock Spectra*

The optical spectra of the shock models in Table 6 display some unusual features. The principal optical emission in these models is the [O III] λ5007 line. The cooling in the oxygen-neon mixtures, with contributions from carbon, magnesium, and silicon is very strong. The other species provide fine-structure cooling mechanisms when the oxygen is at the O II stage, so the mixture is cooler even than the pure oxygen plasmas of Itoh (1981a, b) and [O II] emission is suppressed. The principal contribution of the shock to the overall optical spectra will come from the [O III] λ5007, [O III] λ4959, and [O III] λ4363 lines.

As already mentioned, the shock spectra are not in good agreement with the observations. The $I_{4363}/(I_{5007} + I_{4959})$ ratio in the models of Table 6 is very high, considerably higher than those observed. This clearly indicates that shocks cannot

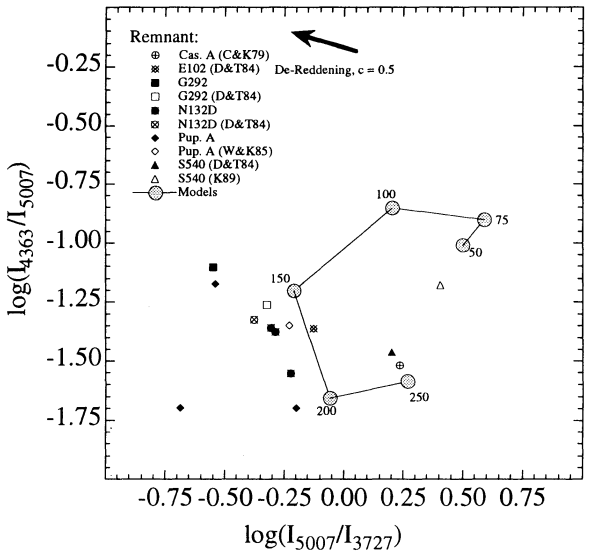

FIG. 13*a*

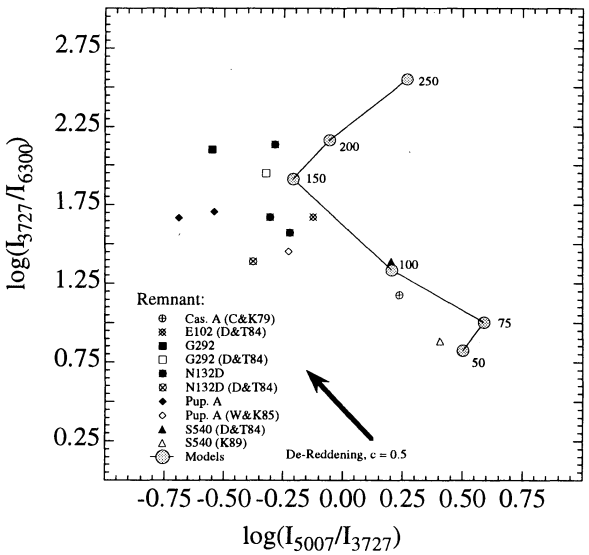

FIG. 13*b*

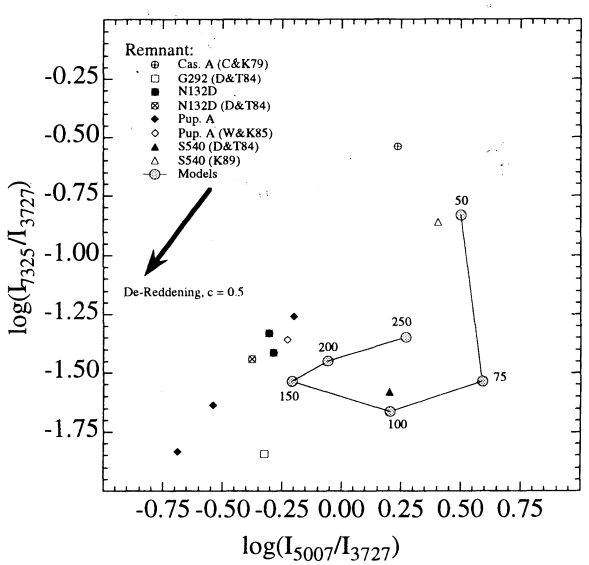

FIG. 13*c*

FIG. 13.—(*a*) Dereddened line ratios of [O III] λ4363, [O III] λ5007, and [O II] λλ3726+29, for combined shock and ionization front models. The OSP150 and OSP200 models bracket the observations of the temperature-sensitive [O III] ratio. Overall the [O II] emission is weak in the models. Observation identifications are given in Table 2. (*b*) As for (*a*), but for [O I] λ63000, [O II] λλ3726+29,, and [O III] λ5007. (*c*) As for (*a*), but for [O II] λλ7320+30, [O II] λλ3726+29, and [O III] λ5007.

be solely responsible for the observed emission. The [O II] and [O I] emission is far too weak in the shock models as well.

7.2. *Combined Spectra*

The optical forbidden oxygen line ratios from the combined shock and ionization front models (models OSP050–OSP250) are compared with observations in Figure 13. The observations are from Table 2, and the model spectra are given in Table 7. Analogously to the diagnostic plots of Paper I, dereddening vectors for the correction due to $c = 0.5$ are shown, to indicate in this case, the direction along which errors in the reddening estimates would have moved the observations.

It is clear from Figure 13*a* that the previously problematic I_{4363}/I_{5007} ratio is now well reproduced in the models. Models OSP150–OSP250 lie in the range defined by the observational points. However, the modeled I_{5007}/I_{3727} ratio is generally greater than the observations. Most of the observations are between the OSP150 and OSP200 models, although the SNR 0540−69.3 observation by Kirshner et al. (1989) and the Cas A observations lie closer to the OPS250 model. The slower shocks, producing models OSP050–OSP100, are a poor fit, due largely to the relatively smaller contribution from the ionization front emission and the consequent dominance of the shock spectrum, which fits the observations very poorly. The low-velocity models have too much [O III] λ4363 emission and not enough [O II] λλ3727, in line with the conclusions of Dopita et al. (1984).

In Figure 13*b* the OSP150 model is once again in the observed range. This consistency gives some credence to the model structure presented here, even with the modeling simplifications adopted. Care should still be taken in the interpretation, as the outliers, Cas A and SNR 0540−69.3, are nearer to the OSP100 model, rather than the faster OSP250 model in the previous plot. In these cases, the observed points are displaced along the direction that might be expected from an increase in density sufficient to quench the [O II] λλ3727 emission. This trend happens to lie along the direction of the velocity progres-

TABLE 6

OXYGEN-RICH SHOCK MODEL SPECTRA ($I_{5007} = 1.000$, $n_0 = 100.0$ cm^{-3})

Transition		Models					
		OS050	OS075	OS100	OS150	OS200	OS250
[OII]	λλ7320+30	0.045	0.003	0.001	0.000	0.000	0.003
[OI]	λ6300	0.000	0.000	0.000	0.000	0.000	0.000
[OIII]	λ5007	1.000	1.000	1.000	1.000	1.000	1.000
[OIII]	λ4363	0.098	0.128	0.151	0.167	0.177	0.177
[NeIII]	λ3869	0.026	0.051	0.063	0.023	0.071	0.294
[OII]	λλ3727	0.132	0.008	0.002	0.001	0.000	0.000
[NeV]	λ3426	0.000	0.001	0.043	0.414	0.621	1.738
$\log(I_{4363}/I_{5007})$		-1.007	-0.894	-0.822	-0.777	-0.751	-0.752
$\log(I_{3727}/I_{5007})$		0.881	2.079	2.629	3.056	3.531	3.479
$\log(I_{7325}/I_{3727})$		-0.469	-0.397	-0.591	-0.530	0.017	1.007
$\log(I_{3727}/I_{6300})$		2.479	2.552	2.488	2.128	1.394	0.692

TABLE 7

FINAL OPTICAL EMISSION SPECTRA ($I_{5007} = 1.000$, $n_0 = 100.0$ cm^{-3})

Transition		Models					
		OSP050	OSP075	OSP100	OSP150	OSP200	OSP250
[OII]	λλ7320+30	0.046	0.007	0.014	0.047	0.041	0.024
[OI]	λ6300	0.047	0.026	0.029	0.020	0.008	0.002
[OIII]	λ5007	1.000	1.000	1.000	1.000	1.000	1.000
[OIII]	λ4363	0.098	0.125	0.140	0.063	0.022	0.026
[NeIII]	λ3869	0.026	0.050	0.062	0.091	0.144	0.142
[OII]	λλ3727	0.315	0.257	0.625	1.617	1.148	0.540
[NeV]	λ3426	0.000	0.001	0.040	0.144	0.052	0.182
$\log(I_{4363}/I_{5007})$		-1.010	-0.903	-0.852	-1.203	-1.656	-1.585
$\log(I_{3727}/I_{5007})$		0.501	0.589	0.204	-0.209	-0.060	0.267
$\log(I_{7325}/I_{3727})$		-0.835	-1.538	-1.663	-1.536	-1.452	-1.348
$\log(I_{3727}/I_{6300})$		0.823	1.003	1.333	1.911	2.162	2.551

sion and the reddening vector. This combines to make the interpretation of these points uncertain, especially given the limitations on the density regime that may be modeled with the present method. This plot is a weak diagnostic tool.

Finally, in Figure 13*c* these same OSP150 and OSP200 models are once again near the main clump of observations, although there is considerable scatter of the observed points along the reddening vector. In addition, the locus of the model points is quite nonlinear, covering a wide range of the I_{7325}/I_{3727} ratio. This highlights the perils of a homogeneous model interpretation of the density diagnostics. On the positive side, the majority of the models do lie in the region where the emission is largely from the homogeneous low-density ionization front zone, as the simple models of Paper I predicted, but the variable density shock contribution can cause strong deviations. The Cas A observation remains an exceptional point, as it lies in a region where at least some high-density material must be contributing to the spectra, and hence may not be modeled accurately here. The SNR 0540−69.3 measurements of Dopita & Tuohy (1984) and Kirshner et al. (1989; which uses spectra from 1982) are in disagreement over the [O II] λλ7320+30 flux, making the interpretation of this remnant difficult as well. The Dopita & Tuohy (1984) value puts the remnant closer to the other OSNR observations, but this may be coincidental. More observations of this remnant are needed.

The correspondence of the observations with the locus of the OSP150–OSP200 models is very encouraging. A general lack of [O II] λλ3727 radiation is predicted, but this may be the result of the optically thin ionization front model assumptions. Otherwise, the fit is very reasonable. The fact that the model parameters were selected by global dimensional considerations, albeit additionally limited by modeling assumptions, and yet points for the resulting models lie in the same general regions of the diagnostic plots as the observational points, is taken as strong support for the emission mechanism outlined here.

One final, general prediction of the models is that, when the emission lines of a species are produced in both the shock and the ionization front, line splitting or broadening up to the shock velocity may be observed, depending on the projection. Other lines that come from only one component, such as [O I] emission from the front or [Ne V] from the shock, should have different velocities. Details of the line splitting are not modeled here and will be the subject of future work.

7.3. *UV Spectrum of* SNR E102.2−7219

The UV observations of Blair et al. (1989) are an important observational data set. A number of points arose from the Blair work. They found that the UV emission is relatively weaker than might have been expected from a simple shock model and that a simple photoionization model is inadequate as well. In addition, the UV resonance lines of carbon and oxygen appear to have strong recombination components. While the MAPPINGS II code does not compute the details of the recombination contribution to the UV carbon and oxygen spectra it still serves to make a comparison of the ionization front mechanism models presented here with the SNR E102.2−7219 data. Table 8 compares the OSP150 and OSP200 models, which were most successful in modeling the optical spectra, with the SNR E102.2−7219 spectra in both the optical and near UV.

The overall fit to the specific SNR E102.2−7219 spectra is quite good in the optical. The modeled UV line spectrum is also generally weak, as observed. Given the observational error of up to 50 times in the UV fluxes by Blair and coworkers, only limited detailed conclusions should be drawn from the models; namely:

1. The modeled Mg II λ2799 emission is brighter than the observed flux, by a factor of 7 or so. Barring a strong contribution from recombination, this suggests that the magnesium level in the initial abundance set was too high, and a [Mg/O] ratio of −2.2 may be more appropriate. This measurement is

TABLE 8

OPTICAL-UV SPECTRUM COMPARISON ($I_{5007} = 1.000$, $n_0 = 100.0$ cm^{-3})

Transition		Observed[a]	Models	
		E102.2-7219.	OSP150	OSP200
[OII]	λλ7320+30	0.090	0.047	0.041
[OI]	λ6300	0.047	0.020	0.008
[OIII]	λ5007	1.000	1.000	1.000
[OIII]	λ4363	0.048	0.063	0.022
[NeIII]	λ3869	0.207	0.091	0.144
[OII]	λλ3727	1.640	1.617	1.148
[NeV]	λ3426	0.108	0.144	0.052
C I]	λ2967	...	0.006	0.001
MgII	λ2799	0.064	0.421	0.431
[Ne IV]	λλ2423	0.183	0.029	0.030
CII]	λ2326	...	0.037	0.015
CIII]	λ1909	0.106	0.019	0.039
[Mg VI]	λλ1806	...	0.011	0.004
OIII]	λ1664	0.084	0.006	0.007
CIV	λλ1549	0.520	0.514	0.080
OIV]	λ1401	0.315	0.071	0.012
SiIV	λλ1397	(incl. above)	0.003	0.001
OI]	λ1357	0.202	0.018	0.016
CII	λ1335	...	0.053	0.044
OV]	λ1218	...	0.694	0.088

[a] Dopita & Tuohy 1984, Blair et al. 1989.

highly uncertain, being based on a single measurement, and should not be taken as definitive.

2. The correspondence between the observed and modeled strengths of the C IV resonance line is good for the OSP150 model, but the line is too weak in the OSP200 model. The agreement for OSP150 may be fortuitous, as recombination contributions have not been included, and the OSP200 model may be a better overall fit.

3. The other strong carbon line, C III] λ1909, which should not have a recombination component, is within a factor of 2.5–5 of the observed flux. The ratio of the line with the C IV resonance line in the two models brackets the observed ratio.

4. Finally, the [Ne III]:[Ne IV]:[Ne V] ratios are not too dissimilar to the observed ratios, given the measurement uncertainties. This gives some confidence in the ionization structures developed here. Neither the optical nor the UV neon emission flux conflicts significantly with the chosen abundance levels of [Ne/O] = −0.34.

8. CONCLUSIONS

The simple ionization front model of D87 has been shown to be feasible in the case where the front is driven by the detailed upstream radiation of a radiative shock traversing a knot of oxygen-rich material. The model structure can form and produce the observed spectra within the global constraints of a bow-shock/cloud-shock model, with reasonable cloud densities, sizes, and velocities. In particular, the problematic I_{4363}/I_{5007} ratio has been reproduced, as a result of the combination of shock and photoionization components in the model. This relatively high [O III] ratio has been maintained, while still retaining some levels of [O I] and [O II] emission, as is observed.

Present modeling still suffers from a number of difficulties, due as to the simplified radiative transfer used as to the uncertain atomic physics. However, it seems reasonable that the proposed structure is possible, and the development of more sophisticated models should be undertaken.

8.1. *Abundances*

The primary aim of this work was to test the feasibility of an emission mechanism. It is clear that the model is indeed feasible, but that a more rigorous radiative transfer method is still needed before really reliable quantitative models become possible. In this context, the details of the composition, beyond some qualitative conclusions, are probably not justified yet.

The abundances of the element with respect to oxygen are not very well constrained by the observations. The optical spectra do not place strong constraints on even the neon abundance because of the sensitivity to the excitation conditions and uncertainties in the models. Nevertheless, the initial abundances of Table 3 do give a good overall fit to the observed spectra and result in a reasonable model structure. The model shock structures depend somewhat on the additional cooling provided by the carbon, magnesium, and silicon ions. The same applies to the photoionization models, where the additional absorption cross sections of these ions is important to the heating achieved. The abundances used, chosen on the basis of massive star evolution models, are therefore generally consistent with the observations.

The [Ne/O] ratio is estimated to be −0.34; the observations do not suggest that this is significantly in error (except for SNR 0540−69.3, of course). Furthermore, the UV spectrum of SNR E102.2−7219 does not give strong indications that the initial ratio of [C/O] of −1.05 is greatly in error, either. The magnesium abundance chosen initially may be too high for the case of SNR E102.2−7219, based on the single Mg II λ2799 measurement. A ratio of [Mg/O] = −2.2 is estimated, with large uncertainty. Nothing in the observations places any reliable limitations on the silicon levels, except on the basis of nondetection in the difficult observations of SNR E102.2−7219. In the present models, the silicon levels would have to be raised a 100-fold, or have a strong recombination contribution in the Si IV $\lambda\lambda$1397 emission line, to come into conflict with the (lack of) observed emission. The uncerrtainties here are too great to warrant any conclusions on Si abundances.

8.2. *Remaining Difficulties*

This examination of the ionization front model supports the view that this mechanism is a reasonable model for the oxygen-rich emission in OSNRs. Having said this, a number of areas in the modeling have, perforce, been simplified or even neglected for lack of data and/or theoretical understanding. Before this model may be used for detailed quantitative measurements, these areas will need to be addressed further.

The total cooling function calculations used here are expected to be reasonably accurate, and the cooling timescales of the shocks should be reliable. The main weaknesses in the computation of the atomic processes lie in the details of the emission-line spectra. The recombination spectra of the heavier ions are not calculated at all. This should not affect the cooling rates very much, as discussed in Sutherland & Dopita (1993), where recombination is shown to *not* be a cooling process in the first approximation. Recombination may only affect the temperature indirectly, by removing selective ranges of electron energies from the existing thermal distribution. The recombination zones of the shock models are already very cool, and any recombination cooling will have little effect in any case. However, the observed resonance lines, particularly the UV resonance lines of carbon, oxygen, and magnesium, can have significant recombination components under the conditions modeled here, and this aspect of spectrum synthesis should be addressed.

Electron conduction was not considered, due to the computational complexity of incorporating such effects into the explicit one-dimensional Lagrangian structures used. Modeling by Borkowski & Shull (1990) of the effects of electron conduction showed that, while there is some effect in the hot zones, in the cooled recombination zones of the shock structures conduction was only significant when the plasma was pure oxygen, and fine-structure cooling was less important. When significant levels of neon, silicon, magnesium, and carbon are introduced, the subsequent fine-structure cooling completely dominates any effects of electron conduction heating. So, electron conduction may not be a serious omission in the oxygen-neon-carbon mixtures used here.

Another important assumption used is the strong coupling of the electron and ion temperatures in the model structures. The present modeling assumes that the electron and ion temperatures are equal for both the shock and ionization front models. Some justification for this may be made for the shock models. There is some observational evidence for rapid electron heating in collisionless shocks (i.e., Pravdo & Smith 1979), possibly due the plasma turbulence in the shock front itself. Therefore, in the face of the general theoretical ignorance of the detailed processes in collisionless shocks (see the review by McKee & Hollenbach 1980), it seemed that the construction of

a two-fluid shock model (electrons and ions) was an unnecessary complication in the already highly simplified model being considered here, especially since electron conduction had been ignored. The earlier work of Dopita & Tuohy (1984) compared results of the equilibrated electron-ion models and separated two-fluid models and found that the shock spectra were very similar when a somewhat higher shock velocity was used for the two-fluid models. It should also be mentioned that the more recent observational test of collisionless shock heating of electrons in Cas A and Pup A, by Jerius & Teske (1988), proved inconclusive so the matter remains an open question.

The effects of molecules and dust are not included in the MAPPINGS II code, as yet, and so could not be included in the modeling. Fortunately, the cool plasmas considered here are unlikely to be molecular, as they are highly ionized by the strong radiation fields present. The effect of dust grains is uncertain, even more so as the dust composition is likely to be abnormal. Dust, if present, might be expected to affect the hot ambient OSNR medium (Dwek 1987; Arendt et al. 1991), but the ambient plasma was taken as an observable and not modeled here.

The last major omission from the atomic processes is charge-exchange reactions involving only heavy atoms. While in normal calculations MAPPINGS II incorporates many exchange reactions, these are all with neutral and ionized hydrogen or helium. The direct reaction rates between ions of oxygen, neon, and carbon are not known , and the complexity of the reaction mechanism rate calculations makes even rough estimations impossible. Dopita et al. (1984) argue that this omission may not be too serious in the shock models considered, since in the zones where charge exchange may be expected, the temperatures are so low that their effect on the emission spectra would be minimal. The effect on the ionization fronts is not so clear however, and the omission of charge exchange in the absence of available data is a caveat that simply has to be borne in mind for the present models, until the atomic data becomes available.

As has been discussed earlier, the simplified modeling neglected the internal photon absorption near the ionization front. This is expected to suppress the low-ionization [O I] and [O II] emission, compared to an actual ionization front. Whether internal absorption will, in practice, maintain higher levels of [O I] λ6300 and [O II] $\lambda\lambda$3727 over a wider range of velocities is not certain and will require more sophisticated modeling. The present models therefore overestimate the excitation and temperatures achieved for a given shock velocity. It is hoped that a fuller radiative transfer treatment will result in the same effects being achieved at a higher velocity than the corresponding models here. The infinite plane-parallel treatment will also tend to overestimate the radiation field, and two- or three-dimensional treatment may be necessary.

8.3. *Future Work*

Overall, the current model is an oversimplification of the physics of the situation. Nonetheless, given the lack of success of previous models, the results obtained here are very encouraging and give confidence that the elements of the correct physics have been identified. In the light of this, the added effort required to address some of the problems outlined above should prove worthwhile. The need for more complete atomic data is apparent, notably charge exchange reactions and recombination data. The effect of the charge exchange reaction, if any, may prove particularly important in the ionization front models because of the density and temperature regimes involved.

Clearly more constraints can be obtained by further observations. In particular, more UV observations of the Magellanic remnants need to be undertaken. The galactic remnants are hopelessly reddened for UV observations, and the Magellanic remnants provide the best chance for this type of observation.

The present modeling then, while producing a good fit to the observations for a given velocity, continues to suffer from only fitting the observations with a relatively narrow range of cloud-shock velocities ($130 \lesssim v_s \lesssim 230$ km s^{-1}). Nevertheless this represents a significant improvement over previous models.

The authors would like to acknowledge use of the UNIX Sun Sparcstation network at Mount Stromlo and Siding Spring Observatories for the computation of the models presented here. One author (R. S. S.) would also like to acknowledge the support of an Australian Postgraduate Research Scholarship during the research of this work.

REFERENCES

Arendt, R. G., Dwek, E., & Petre, R. 1991, ApJ, 368, 474
Axford, W. I. 1961, Phil. Trans. R. Soc., 253(A), 301
Balick, B., & Heckman, T. 1978, ApJ, 226, L7
Binette, L. 1982, Ph.D. thesis, Australian National Univ.
Blair, W. P., Kirshner, R. P., & Winkler, P. F. 1983, ApJ, 272, 84
Blair, W. P., Raymond, J. C., Danzinger, J., & Matteucci, F. 1989, ApJ, 338, 812
Borkowski, K., & Shull, J. M. 1990, ApJ, 348, 169
Braun, R., Goss, W. M., Caswell, J. L., & Roger, R. S. 1986, A&A, 162, 259
Chevalier, R. A. 1975, ApJ, 200, 698
Chevalier, R. A., & Kirshner, R. P. 1979, ApJ, 233, 154
Clark, D. H., Tuohy, I. R., & Becker, R. H. 1980, MNRAS, 193, 129
Clark, D. H., Tuohy, I. R., Long, K. S., Szymkowiak, A. E., Dopita, M. A., Mathewson, D. S., & Culhane, J. L. 1982, ApJ, 255, 440
Danzinger, I. J., & Dennefeld, M. 1976a, ApJ, 207, 394
———. 1976b, PASP, 88, 44
Danzinger, I. J., & Leibowitz, E. M. 1985, MNRAS, 216, 365
Dopita, M. A. 1987, Australian J. Phys., 40, 789
Dopita, M. A., Binette, L., & Tuohy, I. R. 1984, ApJ, 282, 142
Dopita, M. A., & Tuohy, I. R. 1984, ApJ, 282, 135
Dopita, M. A., Touhy, I. R., & Mathewson, D. S. 1981, ApJ, 248, L105
Dwek, E. 1987, ApJ, 322, 812
Fabian, A. C., Willingale, R., Pye, J. P., Murray, S. S., & Fabbiano, G. 1980, MNRAS, 193, 175
Fryxell, B., Müller, E., & Arnett, D. 1991, ApJ, 367 (619)
Goldsworthy, F. A. 1961, Phil. Trans. R. Soc., 253(A), 277
Goss, W. M., Shiver, P. A., Zealey, W. J., Murdin, P., & Clark, D. H. 1979, MNRAS, 188, 357
Hamilton, A. J. S., Sarazin, C. L. S., & Chevalier, R. A. 1983, ApJS, 51, 115
Hughes, J. P. 1987, ApJ, 314, 103
Itoh, H. 1981a, PASJ, 33, 121
———. 1981b, PASJ, 33, 521
Jansen, F. A., Smith, A., Bleeker, J. A. M., de Korte, P. A. J., Peacock, A., & White, N. E. 1988, ApJ, 331, 949
Jerius, D., & Teske, R. G. 1988, ApJS, 66, 99
Johnston, M. D., & Yahil, A. 1984, ApJ, 285, 587
Kahn, F. D. 1954, Bull, Astron. Inst. Netherlands, 12, 187
Kaler, J. B. 1976, ApJ, 31, 517
Kamper, K. W., & van den Bergh, S. 1976, ApJS, 32, 351
Kirshner, R. P., Morse, J. A., Winkler, P. F., & Blair, W. P. 1989, ApJ, 342, 260
Lasker, B. M. 1978, ApJ, 223, 109
Li, H, & McCray, R. 1992, ApJ, 387, 309
Long, K. S., Helfand, D. J., & Grabelsky, D. A. 1981, ApJ, 248, 925
Mathewson, D. S., Dopita, M. A., Tuohy, I. R., & Ford, V. L. 1980, ApJ, 242, L73
McKee, C. F. 1988, in IAU Colloq. 101, Supernova Remnants and the Interstellar Medium, ed. R. Roger & T. Landecker (Cambridge: Cambridge Univ. Press), 205
McKee, C. F., & Cowie, L. L. 1975, ApJ, 195, 715

McKee, C. F., & Hollenbach, D. J. 1980, ARA&A, 18, 219
Mendis, D. A. 1968a, MNRAS, 140, 435
———. 1968b, MNRAS, 141, 409
———. 1969, MNRAS, 142, 241
Murdin, P., & Clark, D. H. 1979, MNRAS, 189, 501
Pravdo, S. H., & Smith, B. W. 1979, ApJ, 234, L195
Schwartz, J., McCray, R., & Stein, R. F. 1972, ApJ, 175, 673
Seward, F. D., & Harnden, F. R. 1984, ApJ, 287, L19
Seward, F. D., & Mitchell, M. 1981, ApJ, 243, 736
Stathakis, R. A., Dopita, M. A., Cannon, R. D., & Sadler, E. M. 1991, in Supernovae, ed. S. E. Woosley (New York: Springer), 95
Stone, J. M., & Norman, M. L. 1992, ApJ, 390, L17
Sutherland, R. S. 1993, Ph.D. thesis, Australian National Univ.
Sutherland, R. S., & Dopita, M. A. 1993, ApJS, 88, 253
Tuohy, I. R., Clark, D. H., & Burton, W. M. 1982, ApJ, 260, L65
van den Bergh, S., & Kamper, K. W. 1983, ApJ, 268, 129
———. 1985, ApJ, 293, 537
Weaver, T. A., Zimmerman, G. B., & Woosley, S. E. 1978, ApJ, 225, 1021
Whitford, A. E. 1958, ApJ, 63, 201
Winkler, P. F., Canizares, C. R., & Bromley, B. C. 1983, in IAU Symp. 101, Supernova Remnants and Their X-ray Emission, ed. J. Danzinger & P. Gorenstein (Dordrecht: Reidel), 245
Winkler, P. F., Canizares, C. R., Clark, G. W., Markert, T. H., & Petre, R. 1981, ApJ, 245, 574
Winkler, P. F., & Kirshner, R. P. 1985, ApJ, 299, 981
Winkler, P. F., Tuttle, J. H. Kirshner, R. P., & Irwin, M. J. 1988, in IAU Colloq. 101, Supernova Remnants and the Interstellar Medium, ed. R. Roger & T. Landecker (Cambridge: Cambridge Univ. Press), 65
Woosley, S. E., Axelrod, T. S., & Weaver, T. A. 1984, in Stellar Nucleosynthesis, ed. C. Chiosi & A. Renzini (Dordrecht: Reidel), 263